UC Irvine
UC Irvine Previously Published Works

Title

Dynamic Model for Understanding Spatial Temperature and Species Distributions in Internal-Reforming Solid Oxide Fuel Cells

Permalink

Journal

ISSN

Authors

Shaffer, Brendan
Brouwer, Jacob

Publication Date

DOI

Copyright Information

Peer reviewed

Dynamic Model for Understanding Spatial Temperature and Species Distributions in Internal-Reforming Solid Oxide Fuel Cells

Brendan Shaffer

Jacob Brouwer[1]
e-mail: jb@nfcrc.uci.edu

National Fuel Cell Research Center,
University of California,
Irvine, CA, 92697–3550

Direct internal reformation of methane in solid oxide fuel cells (SOFCs) leads to two major performance and longevity challenges: thermal stresses in the cell due to large temperature gradients and coke formation on the anode. A simplified quasi-two-dimensional direct internal reformation SOFC (DIR-SOFC) dynamic model was developed for investigation of the effects of various parameters and assumptions on the temperature gradients across the cell. The model consists of 64 nodes, each containing four control volumes: the positive electrode, electrolyte, negative electrode (PEN), interconnect, anode gas, and cathode gas. Within each node the corresponding conservation and chemical and electrochemical reaction rate equations are solved. The model simulates the counter-flow configuration since previous research (Achenbach, 1994, "Three-Dimensional and Time-Dependent Simulation of a Planar Solid Oxide Fuel Cell Stack," J. Power Sources, 49(1), p. 333) has shown this configuration to yield the smallest temperature differentials for DIR-SOFCs. Steady state simulations revealed several results where the temperature difference across the cell was considerably affected by operating conditions and cell design parameters. Increasing the performance of the cell through modifications to the electrochemical model to simulate modern cell performance produced significant changes in the cell temperature differential. Improved cell performance led to a maximum increase in the temperature differential across the cell of 31 K. An increase in the interconnect thickness from 3.5 to 4.5 mm was shown to reduce the PEN temperature difference about 50 K. Variation of other physical parameters such as the thermal conductivity of the interconnect and the rib width also showed significant effects on the temperature distribution. The sensitivity of temperature distribution to heat losses was also studied, showing a considerable effect near the fuel and air inlets. Increased heat transfer from the cell edges resulted in severe temperature gradients approaching 160 K/cm. The dynamic capability of the spatially resolved dynamic model was also demonstrated for a 45% power increase perturbation while maintaining constant fuel and air utilizations. [DOI: 10.1115/1.4006477]

Introduction

Solid oxide fuel cell (SOFC) systems show promise as a future stationary power generation technologies. Given the recent Solid State Energy Conversion Alliance (SECA) improvements [1] this technology is approaching commercial viability at an ever increasing rate. The SOFC ability for direct internal reformation of hydrocarbon fuels, in particular natural gas, provides the incentive of using the existing domestic fuel infrastructure. Integrated SOFC systems can process hydrocarbon fuels and produce electricity and heat by electrochemical reactions that lead to low emissions of pollutants and greenhouse gases. The integrated fuel processing characteristics, especially with internal reformation, allow the co-production of hydrogen or other fuels, which may help introduce emerging hydrogen infrastructure for alternative transportation applications. These qualities make the SOFC especially suited for large scale deployment as a power generation source in an incipient hydrogen economy.

Despite this optimistic outlook, the present situation recognizes several impediments to the reliability of direct internal reforming (DIR)-SOFC technology. The first is coking of the hydrocarbon fuel in the anode compartment. Coking results in the deactivation of reaction sites and clogging of pores and eventually to cell damage (e.g., cracking). Some publications have shown coking to be a minor problem when operating at high temperatures and steam-to-carbon (S/C) ratios [2,3]. However, the focus of much SOFC research has been on the reduction of operating temperature to reduce degradation, improve efficiency, and allow for better seals to be used. The use of high S/C ratios also dilutes the fuel in the anode channel thereby reducing electrochemical performance, and requires water and heat addition (to raise steam). Despite these drawbacks to operating at high temperatures and high S/C ratios, this paper will consider these conditions so as to avoid the issue of coking and to focus upon the second impediment, which is the presence of high thermal stresses caused by steep thermal gradients across the PEN that result from the interacting kinetics of endothermic reformation and exothermic electrochemical reactions in the anode compartment.

A dynamic quasi-two dimensional planar SOFC model is developed for the investigation of thermal gradients within DIR-SOFCs. The finite volume model consists of 64 nodes that each

contain four control volumes. A complete discussion of the model is presented in the following section.

Model

The dynamic DIR-SOFC model is developed in the MATLAB Simulink® platform. The finite volume approach has been dubbed by some as being more appropriate for the modeling of SOFCs because it may approximate the physical processes better [4]. The finite volume approach is one way (versus the finite element approach) to implement the method of lines where all but one dimension of the governing partial differential equations are discretized. In this manner, all the spatial dimensions are discretized leaving a system of ordinary differential equations in time for which numerical solvers are numerous.

The cell was divided into 64 nodes as presented in Fig. 1. Each node consists of four control volumes: the interconnect, anode and cathode compartments, and the PEN. The dimensions of these control volumes are as defined in Figure 2 and Table 1.

The assumptions used in the current model are similar to those used by Mueller et al. [5], which include the following:

(1) The fuel cell is well insulated such that heat loss from the cell is negligible.
(2) The flow in the fuel cell is laminar.
(3) Pressure drops are negligible.
(4) The gases are ideal and incompressible.
(5) Radiation heat transfer is negligible [6,7].
(6) Conduction along the PEN is negligible since conduction through the interconnect dominates.
(7) Coking is negligible due to the high steam to carbon ratio used in the following analyses [2,3].
(8) The water gas shift reaction is assumed to be in equilibrium.
(9) Both electrodes exhibit high enough conductivity that it is assumed that both are an equi-potential surface.
(10) Only hydrogen participates in the electrochemical reaction at the anode.
(11) The electrochemistry is rapid such that the rate of reaction is proportional to the current.

The cell is in the counter-flow configuration as shown in Fig. 1. This flow configuration has been shown to have the lowest temperature difference across the cell [8]. For the purposes of plotting, the direction of fuel flow designates the direction of the abscissa axis.

Electrochemical Model. The equipotential assumption allows the input of a cell voltage for which the electrochemical model locally calculates the current such that the specified cell voltage is met. The electrochemical performance is governed by the equation for cell voltage shown below:
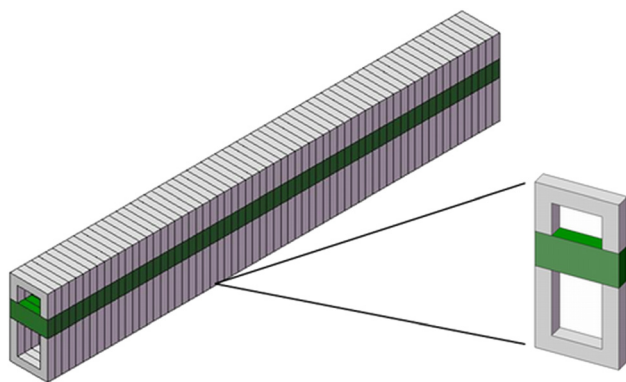

Fig. 1 Schematic of the solid oxide fuel cell model

$$V = E_{\mathrm{OCV}} - \eta_{\mathrm{act}} - \eta_{\mathrm{ohm}} - \eta_{\mathrm{conc}} \qquad (1)$$

The first term in Eq. (1) is the Nernst voltage calculated using the following equation:

$$E_{\mathrm{Nernst}} = E_0 - \frac{R_u T_{\mathrm{PEN}}}{nF} \ln\left(\frac{P_{\mathrm{H_2O}}}{P_{\mathrm{H_2}} P_{\mathrm{O_2}}^{1/2}}\right) \qquad (2)$$

The first term in the Nernst equation is the reversible potential and is calculated from the Gibb's free energy using the equation and polynomial below:

$$E_0 = -\frac{\Delta G}{nF}$$

$$\Delta G = (-2.4087E - 9 \cdot T_{\mathrm{PEN}}^3 + 1.0641E - 5 \cdot T_{\mathrm{PEN}}^2$$

$$+ 0.0411 \cdot T_{\mathrm{PEN}} - 241.9459) \cdot 1000 \qquad (3)$$

The second term represents what has been termed the Nernstian losses. These losses are a result of the bulk reactant concentrations present at each location along the anode and cathode channels. The Nernst voltage corresponds to the voltage of the cell at open circuit conditions without current leakage across the electrolyte or anode/cathode gas leakage. The other terms in the equation for the cell voltage approximate the electrochemical dynamics as summarized by three bulk loss terms: activation, concentration, and ohmic polarization. The activation polarization results from the existence of an activation barrier at each electrode that the electrochemical reactions must overcome to proceed at a certain rate. This barrier is surmounted by the use of some of the chemical potential difference that would otherwise contribute to a voltage difference to sufficiently lower the activation barrier. Using the Butler-Volmer model of activation polarization and assuming that the activation losses occur only at the cathode and are symmetric (i.e., transfer coefficient of 0.5), the following equation can be derived:

$$\eta_{\mathrm{act}} = \frac{2R_u T_{\mathrm{PEN}}}{nF} \sinh^{-1}\left(\frac{I}{2j_0 A}\right) \qquad (4)$$

This approximation of activation losses is usually sufficient in an SOFC system model because activation losses are fairly low and usually dominated by one electrode (the cathode). However, the above equation is a semi-empirical equation for which the exchange current density parameter, j_o, is usually empirically determined from experiments such that a fit to an experimental V-I curve is obtained by the model. Therefore, although the activation polarization equation has its roots in first principles, the practical use of the equation typically requires some empirical curve fitting, which may include other parameters in addition to the exchange current such that a reasonable approximation to experimental performance is obtained.

The concentration polarization results from a lack of sufficient supply of reactants to the triple phase boundary such that the reaction occurs at a reduced rate for a given voltage difference. This loss ultimately results in the failure of the cell's ability to produce power. As more power is demanded from the cell, the reactants at the triple phase boundaries decrease until there are so few reactants present at the TPBs that the cell no longer produces current. The current density at which this occurs is termed the limiting current density. The equation describing this voltage loss mechanism is:

$$\eta_{\mathrm{conc}} = -\frac{R_u T_{\mathrm{PEN}}}{nF} \ln\left(1 - \frac{I}{j_L A}\right) \qquad (5)$$

where j_L is the limiting current density, A is cell area, and F is Faraday's constant.

Ohmic polarizations are those losses due to electronic and ionic resistances within the cell (e.g., electrolyte resistance to ion flow, electrode-electrolyte interfaces) and the cell assembly (e.g., interconnect and current collector electron flow resistances, contact resistances between the cells and interconnects). The ohmic resistance of the cell that is used in this work was adapted from the experimental data given by Kim et al. [9]. The following equations are used in the current cell model:

$$\eta_{\text{ohm}} = i R_{\text{PEN}}(T_{\text{PEN}}) \tag{6}$$

$$R_{\text{PEN}} = T_{\text{PEN}} \cdot e^{C1/T_{\text{PEN}}+C0} \tag{7}$$

Reformation Reactions. The direct operation of the SOFC on natural gas requires the model to account for the reformation reactions and the kinetics associated with them. The natural gas is assumed to be pure methane in this paper. The following reactions are the steam methane reformation (SMR) reaction and the water gas shift (WGS) reaction:

$$CH_4 + H_2O \rightarrow CO + 3H_2 \tag{8}$$

$$CO + H_2O \rightarrow CO_2 + H_2 \tag{9}$$
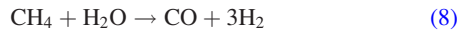
SMR is endothermic and the WGS reaction is slightly exothermic (when H_2O is steam); however, their typical combined contribution to heat generation under SOFC anode conditions is quite highly endothermic. The possibility of balancing this internal reforming endothermicity with the exothermicity of the electrochemical reaction was one of the original motivations for investigating direct internal reformation [8].

A number of attempts to assess empirical expressions accurately depicting SMR kinetics have been performed. Some of these experimental studies did not use materials germane to solid oxide fuel cell anodes [10]. Earlier DIR-SOFC publications such as Aguiar et al. [11] used kinetic data from Achenbach and Riensche [12], citing that their data was typical of SMR on SOFC anodes. The expression below for SMR reaction rate is garnered from Ref. [12]:

$$R = \pm\nu k_0 P_{\text{CH}_4} A \left(1 - \frac{Q}{K_{eq}}\right) e^{-E_a/R_u T} \tag{10}$$

In the above equation, R is the rate of reaction; the coefficient ν is the stoichiometric coefficient of the particular species involved in the reaction, the pre-exponential factor k_0 is 4.274 kmol/(m²-s-bars), the partial pressure of methane is P_{CH_4} in bars, A is the surface area of the node, Q is the reaction quotient, K_{eq} is the equilibrium constant, the activation energy E_a is 82,000 kJ/kmol, the universal gas constant R_u is 8.314 kJ/(kmol-K), and T is the temperature of the node.

The water gas shift reaction is assumed to be at equilibrium as mentioned previously. Ahmed and Foger [13] examined this assumption experimentally in their 2001 publication and found it to be reasonable for typical SOFC conditions and at high levels of fuel utilization. For low levels of fuel utilization, it was found that the WGS reaction did not approach equilibrium. The rate of reaction for the WGS reaction used in the present study is shown below

$$R = \pm\nu k_0 P_{CO} A \left(1 - \frac{Q}{K_{eq}}\right) \tag{11}$$

This equation was adapted from Aguiar et al. [11]. The pre-exponential constant, k_0, is a number large enough such that the rate of reaction equation produces near equilibrium conversion.

Conserved Quantities: Mass and Energy. Mass and energy conservation equations are used in the current model. Momentum is conserved by the assumption of constant pressure. This assumption has been shown by other publications to achieve results similar to those models that solve momentum conservation equations that can determine pressure losses [14]. The use of this assumption allows a substantial reduction in computational intensity that is appropriate for the dynamic system level model developed herein. The conservation equations of mass and energy have different characteristic times associated with them depending upon the particular control volume they are describing. For example, the cathode compartment experiences much higher flow rates than the anode compartment, resulting in different residence/characteristic times. To avoid these issues associated with differing characteristic times, a variable time step solver was used. The variable time step solver selects a period that is below the smallest characteristic time so that it might well and simultaneously solve all of the integral conservation equations.

Mass. Within each gas control volume the total number of moles is conserved using the equation:

$$\frac{dN}{dt} = \dot{N}_{\text{in}} + \sum R - \dot{N}_{\text{out}} \tag{12}$$

This equation written for an individual species is:

$$\frac{d}{dt}(N X_{\text{out}}) = \dot{N}_{\text{in}} X_{\text{in}} + R - \dot{N}_{\text{out}} X_{\text{out}} \tag{13}$$

Invoking the perfectly stirred reactor assumption, where diffusion fluxes are ignored, the properties at the exit of each CV may be assumed to be equivalent to the properties of the entire CV. With this perfectly stirred reactor assumption and the assumption that

$$\frac{d(N X_{\text{out}})}{dt} \cong N \frac{d(X_{\text{out}})}{dt} \tag{14}$$

Equation (13) can be manipulated such that an integration in time can be performed for the concentration of the species at the exit and hence within the entire CV.

$$X_{\text{out}} = \frac{R_u T_{\text{out}}}{PV} \int \left(\dot{N}_{\text{in}} X_{\text{in}} + R - \dot{N}_{\text{out}} X_{\text{out}}\right) dt \tag{15}$$

where

$$N = \frac{PV}{R_u T_{\text{out}}} \tag{16}$$

because all gases considered in this model are ideal.

Energy. The conservation of energy is applied to the five CVs, which consist of two different phases of matter: solid and gas. The interaction between the phases is through convective heat transfer only using Newton's Law of Cooling to model this process.

$$\dot{Q}_{\text{conv}} = h A_i (T_i - T_{\text{out}}) \tag{17}$$

The convection heat transfer coefficient, h, is determined using the equation for the Nusselt number. The Nusselt number for the typical dimensions of the gas channels in the fuel cell is 3.8 [15].

$$h = \frac{k}{D_h} Nu \tag{18}$$

The hydraulic diameter is defined as four times the cross sectional area of the flow divided by the wetted perimeter. The thermal conductivity of the gas is calculated using the following approximation:

$$k = \sum X_i k_i(T_{out}) \tag{19}$$

Radiation is assumed to be negligible for the current cell geometry due to the small view factors associated with surfaces of significantly varying temperature. The solid CVs interact energetically through conductive heat transfer modeled using Fourier's Law.

$$\dot{Q}_{cond} = kA \frac{\Delta T}{L} \tag{20}$$

PEN

Application of conservation of energy to the PEN yields the following:

$$\frac{dU_{PEN}}{dt} = \dot{E}_{gen} + \sum \dot{Q} \tag{21}$$

The change in the internal energy of the PEN control volume is equivalent to the sum of the heat transferred to the CV and the heat generated within the CV. The heat generated within the PEN results from the exothermic electrochemical reaction occurring at its TPBs. The heat generated can be described by the following:

$$\dot{E}_{gen} = R_{O_2} h_{O_2}(T_{out}) + R_{H_2O} h_{H_2O}(T_{PEN}) + R_{H_2} h_{H_2}(T_{out}) - IV \tag{22}$$

Since the PEN is a solid (although porous in the electrodes), the specific heat is constant, leading to the equation:

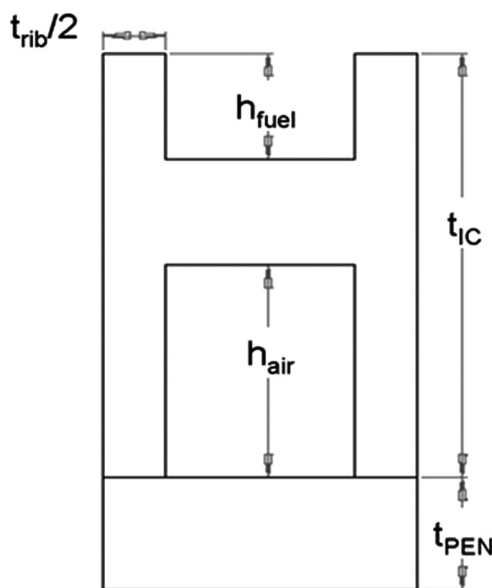$$T_{PEN} = 1/\rho_{PEN} c_{PEN} V \int \left(\dot{E}_{gen} + \sum \dot{Q} \right) dt \tag{23}$$

Interconnect. The interconnect temperature is solved for in the same manner as the PEN except for zero heat generation within the interconnect. The conservation of energy renders the following:

$$\frac{dU_{int}}{dt} = \sum \dot{Q} \tag{24}$$

The internal energy of the interconnect control volume depends simply upon the heat transferred to/from it. As in the case of the PEN, the temperature of the interconnect can be calculated by integrating the sum of the heat transfers in time and dividing that by the product of the density, specific heat, and volume.

Anode and Cathode Gases. The general equations of these two control volumes are identical. Conservation of energy results in the following:

$$\frac{dU}{dt} = \dot{H}_{in} + \dot{H} - \dot{H}_{out} + \sum \dot{Q} \tag{25}$$

Since the anode and cathode gases are assumed to be ideal gases the internal energy is a function of only temperature; hence

$$dU = Nc_v dT \tag{26}$$

Assuming that the anode and cathode gases are ideal gases allows the calculation of the temperature of the control volume.

$$T = \frac{R_u T}{PV c_v(T)} \int \left(\dot{H}_{in} - \dot{H}_{out} + \sum \dot{Q} \right) dt \tag{27}$$

Electrochemical Parameter Determination

The Solid State Energy Conversion Alliance (SECA) performance improvements have been considerable over the last decade as shown in Fig. 3. These performance improvements may have an impact on the thermal and concentration gradients within the cell. These impacts will be investigated by adjusting the electrochemical model parameters such that the experimental data from these better performing cells is matched by the model. These electrochemical model parameters include the exchange current density, the C0 constant in the temperature dependent resistance equation, and the limiting current density. The experimental data used in the current work are from a presentation at the 9th SECA Workshop and are representative of Versa Power SOFCs [16]. While some data show even better performance than the Versa Power data, the information accompanying these data is limited.

Fig. 2   Fuel Cell Dimensions

Table 1   Model parameters

Parameter	Value	Units
PEN thickness	1.06	mm
PEN density	5900	kg/m^3
PEN specific heat	0.5	$kJ/kg \cdot K$
PEN thermal conductivity	2	$W/m \cdot K$
IC thickness	4	mm
IC density	9000	kg/m^3
IC specific heat	0.62	$kJ/kg \cdot K$
IC thermal conductivity	25	$W/m \cdot K$
C1	7509.6	
Cathode channel ht.	2	mm
Anode channel ht.	1	mm
Cell width	0.25	cm
Cell length	10	cm
Cell active area	2.5	cm^2

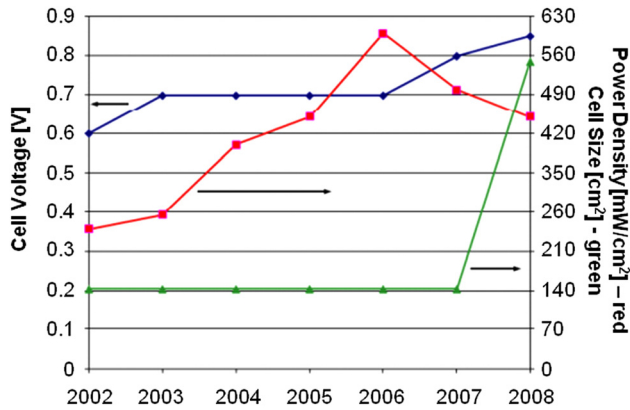**Fig. 3   SECA improvements (taken from Ref. [1])**

Table 2   Operating conditions for Versa Power cell

Operating temperature	973 K
Active area	81 cm^2
Fuel flowrate	2 SLPM
Air flowrate	2 SLPM
V_{cell}	0.85 V
j_{cell}	740 mA/cm^2

Table 3   Performance parameters for Table 2 operating conditions

	High	Low	Units
j_o	2700	1000	A/m^2
C0	−25.94	−25.855	(−)
j_L	35,000	35,000	A/m^2

Therefore it was decided to use the Versa Power data, which includes flow rates. The operating conditions for these data are shown below in Table 2.

The concentration loss was approximated so as to reasonably represent the losses corresponding to the utilizations of fuel and air. The same limiting current density was used in the high and low performance cell simulations. The high performance experimental data was matched by adjusting only the exchange current density and the C0 constant in the temperature dependent resistance equation. Table 3 summarizes the parameters used for the high and low performance cells.

The low performance cell was characterized using typical electrochemical model parameters found in the literature [9,17,18]. The parameters of Table 3 have been used to simulate operation on humidified hydrogen at a temperature of 700 °C with low fuel and air utilizations. The focus of this paper is investigation of direct internal reforming at realistic operating conditions. Therefore, a higher operating temperature range of 1123–1173 K is selected for lower ohmic losses and to avoid extensive coking [2,3]. As the temperature increases, so too will the exchange current density. The exchange current densities used for the high and low performance cells at these increased temperatures are 5000 A/m^2 and 2000 A/m^2, respectively. The low performance (LP) cell exchange current density was selected from the literature with the high performance (HP) cell value adjusted roughly proportionally. Table 4 shows the final fuel cell parameters for higher temperature operation. Note that the higher fuel and air utilizations resulted in lower limiting current density. The limiting current density was approximated based upon the corresponding

Table 4   Performance parameters for operating temperature of 1123–1173 K

	High	Low	Units
j_o	5000	2000	A/m^2
C0	−25.94	−25.855	(−)
j_L	17000	17000	A/m^2

Table 5   Fuel compositions

	No pre-reforming	Partial pre-reforming	Syngas
CH_4	0.25	0.091	0.17
CO	0	0.017	0.05
CO_2	0	0.089	0.215
H_2	0	0.405	0.125
H_2O	0.75	0.398	0.391
N_2	0	0	0.049
T_{inlet}	973	923	948

Table 6   Operating conditions for fuel composition variation simulations

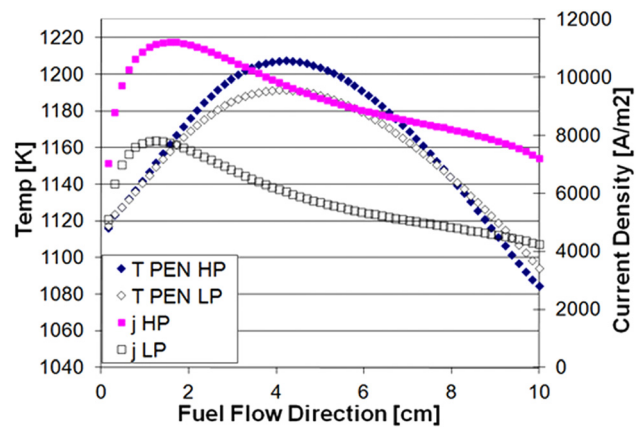| Avg. PEN temperature	1123–1173 K
Fuel utilization	0.85
Air utilization	0.25
V_{cell}	0.7 V

Fig. 4   No pre-reforming, PEN temperature and current density distributions

utilizations. Throughout the rest of the paper these values are used in the simulations unless otherwise stated.

Analysis, Results, and Discussion

Performance and Fuel Composition Variation. The fuel compositions of Table 5 were analyzed for both the high and low performance cells. The partial reformation composition was determined by assuming that the fuel mixture was in equilibrium at 800 K. The syngas composition was determined from NETL data. The inlet temperatures for the air and fuel flows were varied so that the average PEN temperature was maintained within 1123–1173 K.

The operating conditions for the simulations using these fuel composition variations are shown in Table 6.

No Pre-Reformation Case. The no pre-reformation simulations confirmed that the electrochemical performance does have
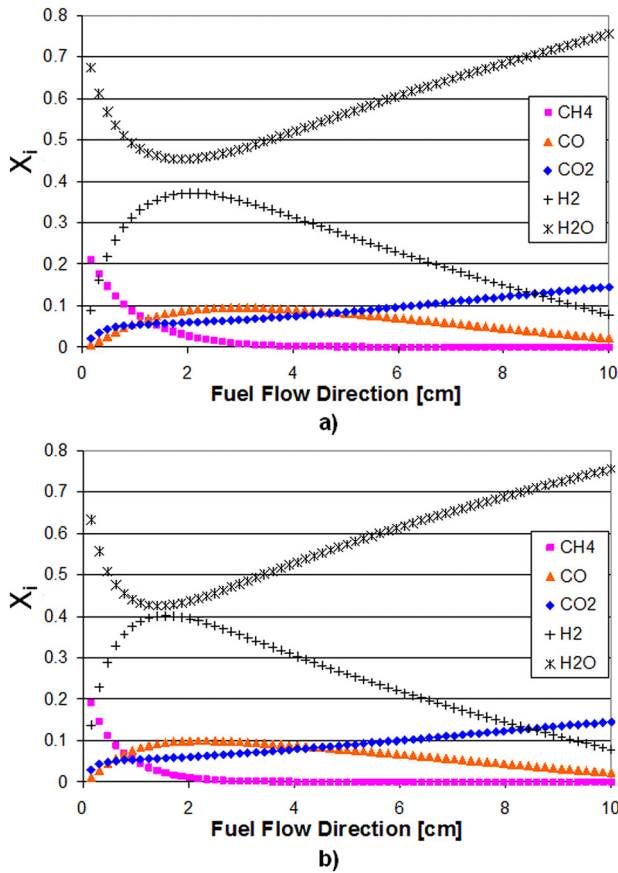
Fig. 5 No pre-reforming, concentration distributions for (a) high and (b) low performance cells
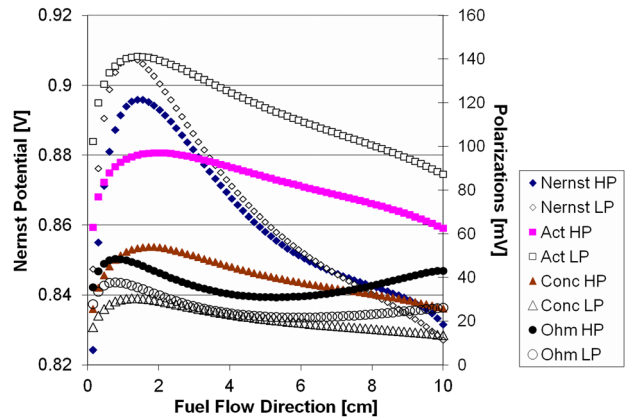

Fig. 6 No pre-reforming, Nernst potential and polarization distributions

Fig. 7 Partial pre-reformation, PEN temperature and current density distributions

an effect on the PEN temperature. In Fig. 4, the peak temperature of the high performance cell increased about 20 K while the average PEN temperature only increased by about 5 K. There is also a disparity in the magnitude of the ΔT_{PEN} across the cell. The increased performance has increased this value by about 25 K. The general shape of the two temperature and current distributions remains similar. Also expected is the increased current density of the high performance cell. As the cell produces more current, more heat is generated leading to the increased ΔT_{PEN} in the high performance case. The PEN temperature near the fuel exit is interesting in that the HP PEN temperature has decreased below that of the LP PEN. This is due to the increased air flow rate in the HP case such that an air utilization of 0.25 is maintained. This increased flow contributes to increased cooling at the fuel exit/air inlet.

Figure 5 shows the species concentration distributions for the HP and LP cells. In both cells, the SMR reactions consume methane and water in the first 2 cm of the cell to produce CO and H_2. The methane is almost fully consumed in the first 2 cm. Within this first 2 cm, the WGS reaction consumes water and the CO produced by the SMR reaction to then produce CO_2 and more H_2. In the remaining 8 cm of the cell, the electrochemical reactions dominate the H_2 and H_2O concentration distributions; water is produced while the H_2 is consumed. Additionally, the WGS reaction controls the CO and CO_2 concentration distributions in the last 8 cm by continuously shifting CO to CO_2. As expected, the HP cell electrochemically reacts more H_2 to produce higher concentrations of H_2O and lower concentrations of H_2 than those of the LP cell. In addition, the methane concentrations in the LP cell are lower than those of the HP cell. The CO concentrations are lower in the HP cell. These results are due to the difference in the rates of electrochemical reaction between the two cells because the rate
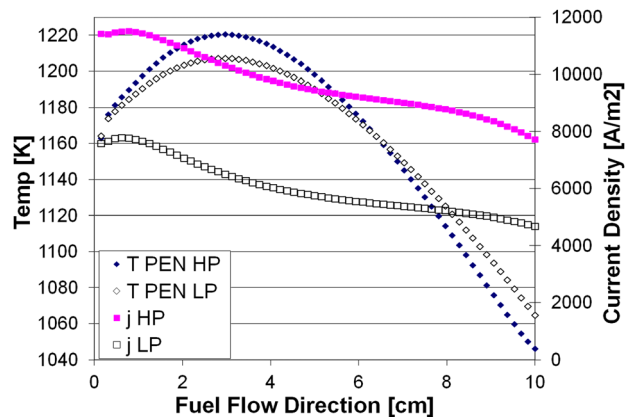
of the SMR reaction in both cells is similar due to similar temperatures and concentrations in this region.

Figure 6 shows the Nernst voltage and polarization distributions. The lower performance cell has a larger peak Nernst potential, which is due in part to the lower peak temperature of the LP cell. The activation losses of the HP cell are much lower than those of the LP cell as expected. The ohmic losses are greater in the HP cell than in the LP cell despite the improvements to the HP cell's resistance and the higher temperatures of the HP cell. This is due to the fact that as the current increases the voltage drop associated with the ohmic losses increases according to Ohm's law. Since the limiting current density was assumed to be equivalent in both cases, the concentration losses are higher in the HP cell because it is operating closer to the limiting current density since in the HP case there is higher current generation.

Partial Pre-Reformation Case. Figure 7 shows the HP and LP cells operating with partially pre-reformed methane. The PEN temperature distributions in this case are contrasted with those of the no pre-reformation case because there is much less endothermic cooling available since there is a lower concentration of methane at the fuel inlet. The dominant cooling mechanism in this case is the convective cooling by the cathode air. The differences between the HP and LP cells are similar to the differences present in the no pre-reformation case. The HP cell has a higher peak temperature as well as a higher current density distribution. The PEN temperature distributions are similar in shape with the PEN temperature near the fuel exit being lower in the HP case due to
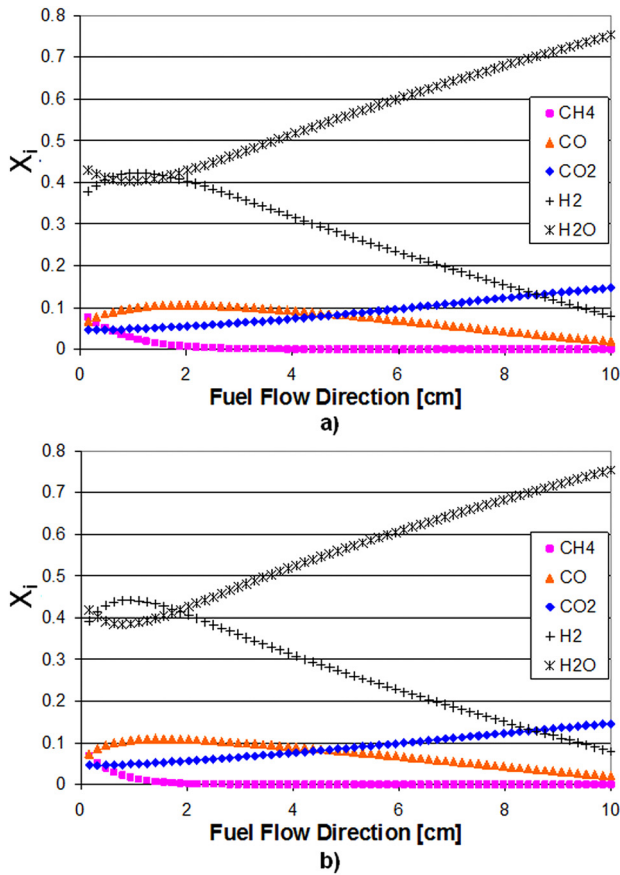
Fig. 8 Partial pre-reforming, concentration distributions for (*a*) high and (*b*) low performance cells
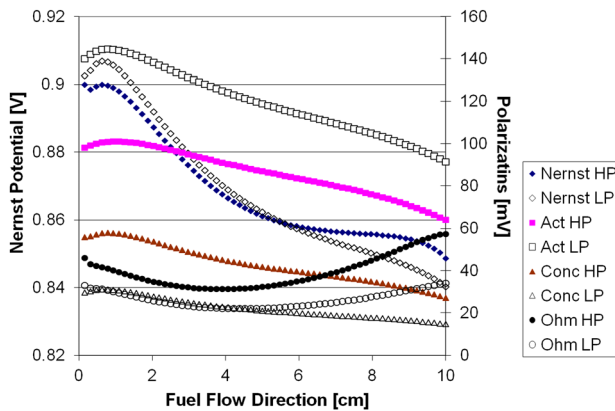

Fig. 9 Partial pre-reformation, Nernst potential and polarization distributions

Table 7 Fuel composition variation summary

	HP			LP		
	NoPreRef	PartPreRef	Syngas	NoPreRef	PartPreRef	Syngas
U_f	85	85	85	85	85	85
U_a	25	25	25	25	25	25
V_{cell} (V)	0.7	0.7	0.7	0.7	0.7	0.7
Icell (A)	2.32	2.42	2.28	1.47	1.50	1.42
T_{PEN} avg (K)	1165	1166	1165	1159	1165	1160
T_{PEN} max (K)	1207	1221	1211	1192	1207	1194
T_{PEN} min (K)	1084	1046	1071	1094	1065	1084
ΔT_{PEN} (K)	123	174	139	97	143	110

the Nernst potential increases in the HP cell surpassing that of the LP cell. This also occurred in the no pre-reformation case but to a lesser extent. The other polarization distributions are similar to the case of no pre-reformation.

Syngas Operation Case. The results obtained for simulating operation on the syngas fuel composition of Table 5 showed that performance characteristics for syngas operation were similar to those of non-reformed and partially pre-reformed methane. Again, the same contrasts were observed between the HP and LP cells: higher max PEN temperature in the HP cell, larger ΔT_{PEN} in the HP cell (by about 29 K), lower PEN temperature near the fuel exit in the HP case, and higher current density distribution in the HP cell. The species concentration and polarization distributions for the HP and LP cells also exhibited similar trends for syngas operation as those presented for the non-reformed and partially pre-reformed methane operation cases.

Table 7 summarizes some of the results from all three fuel compositions for ease of comparison. When there is more hydrogen present in the fuel, the current density and activation polarization distributions are flatter near the fuel inlet, which is expected. The convective cooling of the cathode gas is most pronounced at the fuel exit/air inlet. The average PEN temperatures for all of the fuel compositions simulated are similar. The maximum PEN temperature occurs closer to the fuel inlet for a higher fuel inlet hydrogen content. The higher the hydrogen content the more severe the ΔT_{PEN} and the maximum PEN temperatures become. In the partial pre-reforming case, this is probably due mostly to the increase in electrochemical activity (i.e., higher current) compared to the no pre-reforming case. However, this cannot explain the same trend in the syngas case where a lower current than the no pre-reforming case is observed while a larger max PEN temperature and ΔT_{PEN} are observed in the syngas case compared to the no pre-reforming case. Looking at the max T_{PEN} for the no pre-reforming case and the syngas case again, one should see that they are very similar; however, the min ΔT_{PEN} for both these cases differs by a larger margin. This difference of the min T_{PEN} is due to the increased sensible cooling capability in the syngas case caused by the presence of nitrogen in the fuel, which lowered the min T_{PEN}. These trends show that the fuel composition can also affect the PEN temperature distribution. However, these PEN temperature distributions can be managed through control schemes such as varying the air flow rate such that a constant cathode exhaust temperature is maintained. One could also vary other parameters such as fuel utilization or fuel composition.

Results from this model compare well to similar results in the literature. The concentration distributions agree with those of Aguiar et al. [11], for example. The PEN temperature distributions in the literature, however, exhibit steeper gradients than what is depicted here. Comparisons to Ref. [11] show a slight disagreement near the fuel inlet for their corresponding counter-flow model. Their results show a slight dip (or plateau) in the PEN temperature near the fuel inlet, which then gives way to a distribution
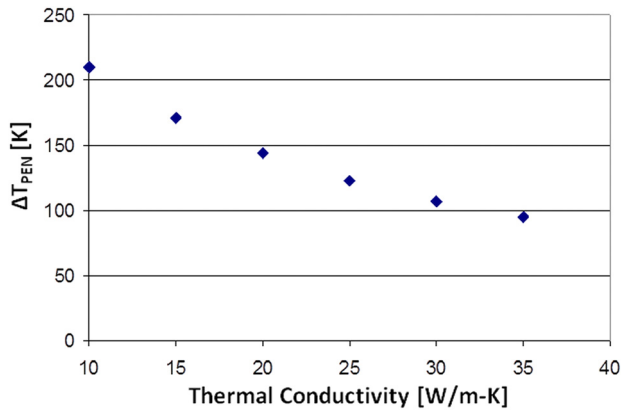
the increased air flow rate. The ΔT_{PEN} in the HP cell is larger than that in the LP cell by about 30 K.

The species concentration distributions for the partial pre-reformation case are shown in Fig. 8. Methane and water are consumed by the reformation and WGS reactions primarily in the first 2 cm of the cell producing hydrogen, CO, and CO_2. Further along the cell, the water concentration rises as the hydrogen is electrochemically consumed. Also, as before, the hydrogen concentration distribution is lower in the HP case, as expected.

Figure 9 shows the Nernst potential and polarization distributions along the cell. The Nernst potential is higher in the LP cell case at the fuel inlet, but as the cell cools due to the cathode air,

Fig. 10 Sensitivity of maximum cell temperature difference (DTPEN) to interconnect thermal conductivity
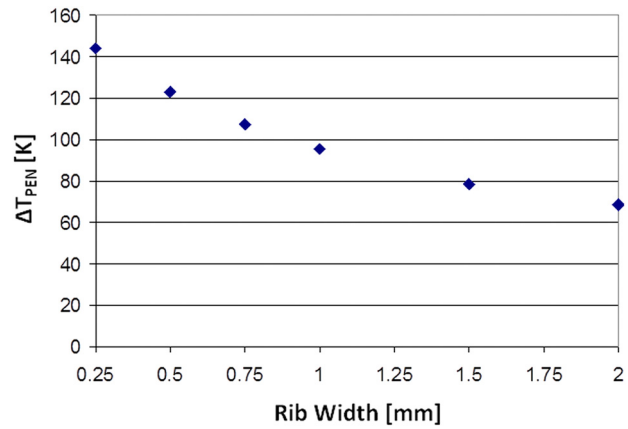

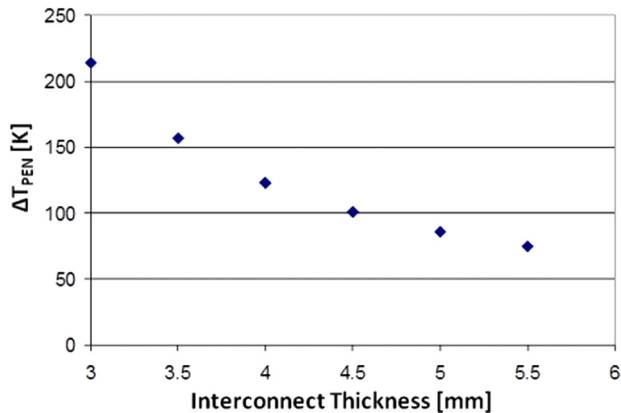**Fig. 12 Sensitivity of maximum cell temperature difference (DTPEN) to rib width**

Fig. 11 Sensitivity of maximum cell temperature difference (DTPEN) to interconnect thickness

similar to the one shown here but with a sharper peak. However, they use a different fuel composition and a different electrochemical model among other things, but the most important difference is the difference in their cell dimensions and interconnect thickness. The cell they modeled was 40 cm long, four times the length of the cell shown here. With a longer cell, a larger maximum PEN temperature difference would be expected. The interconnect thickness as shown in the next section of this paper will also affect this. Furthermore, a rough comparison to the modeling work done by Achenbach [8] shows that the trends presented here agree with the results of that particular study. The results of Achenbach [8] coincide with the PEN temperature trend present near the fuel inlet with no slight dip or plateau rather a sharp increase in PEN temperature. The cell dimensions used in Achenbach [8] were the same as those used here. The fuel composition is different from that used here, and other details such as the interconnect thickness are not specified by Achenbach [8]. It is difficult to make any direct comparison with the models in literature, but the results shown here present similar trends to other publications with similar model assumptions and operating parameters.

Sensitivity to Physical/Dimensional Parameters. The literature does not contain many SOFC simulations that demonstrate the sensitivity of results to the physical and dimensional parameters of the cell. In this section, the interconnect thickness and thermal conductivity are adjusted to explore the effect on the maximum cell temperature differential, a result that is important to resolve for performance and degradation characteristics. The fuel

composition and the corresponding inlet temperatures were specified by the no pre-reforming case. The HP cell parameters were also used for these variations. Figure 10 and Fig. 11 show the results. The interconnect and thermal conductivity both have a marked effect on the cell temperature differential. This is expected considering that as the IC thickness or thermal conductivity is increased, the resistance to heat transfer is decreased thereby allowing heat generated in a hot part of the cell to be transferred to a cool part of the cell more easily. This trend is evidenced by a decrease in the total cross cell temperature difference with increasing interconnect thickness or conductivity. These results suggest that DIR-SOFCs should be constructed using high conductivity (e.g., metallic) interconnects that have a considerable thickness so that severe thermal gradients can be avoided. Increases in thermal conductivity and IC thickness begin to lose their effectiveness in reducing the total cell temperature difference as they approach larger values of 30 W/m-K and 5 mm, respectively. At these values, whatever costs are associated with increasing these parameters may outweigh the benefits of reducing the temperature differential.

The variation of other physical parameters such as the specific heats and densities of the PEN and interconnect did not result in any noticeable effect on the temperature profile. However, variation of the rib width did produce a considerable effect (See Figure 12). The reason behind this effect is similar to the one behind the interconnect thickness and thermal conductivity. By increasing the rib width, the thermal resistance to heat transfer into the interconnect is reduced which allows for an easy flow of heat from hot spots to cool spots hence easing large thermal gradients. However, this model does not consider the pressure effects of increasing the rib width (decreasing cross sectional area of the flows) or the effect of the rib width has on the convective heat transfer properties of the flows since the Nusselt number, which is assumed constant, will change with varying rib width. Therefore, the conclusions from the variation of rib width are not fully reliable and/or complete.

Heat Loss Sensitivity. The inclusion of cell heat loss to the environment has been analyzed in order to assess the sensitivity of model results to this assumption. The heat loss model assumes that the heat loss occurs only at the edges of the cell where fuel and air enter and exit. The fuel used in this analysis was the no pre-reformation case, and the performance used was that of the HP case. The temperature to which the cell edge was transferring heat was varied from 850 to 950 K in order to determine the sensitivity of the model to this parameter. Note that this temperature corresponds to the inside vessel temperature, which through insulation and vessel materials eventually transfers heat to the environment.
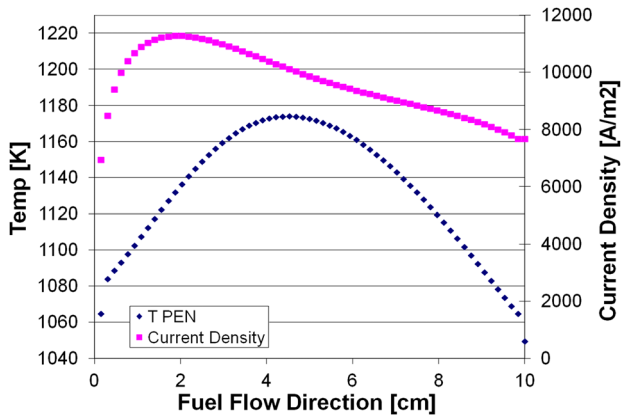
Fig. 13 Effect of edge heat loss with ambient temperature of 950 K on the PEN temperature and current density distributions
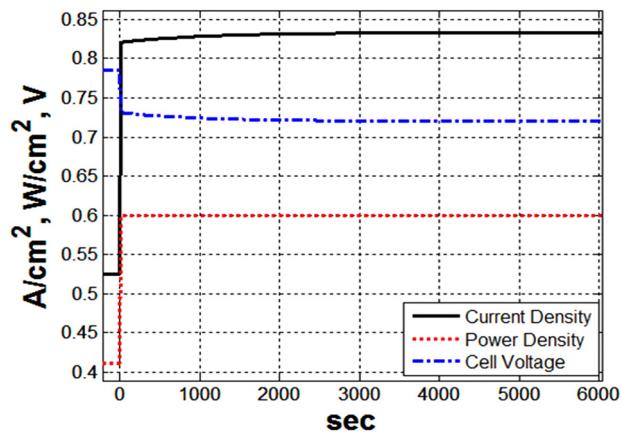

Fig. 15 Response of anode and cathode gas exit temperatures to the 45% power increase

Fig. 14 Current density, power density, and cell voltage during power increase

Fig. 16 Response of minimum, maximum, and average PEN temperatures to the 45% power increase

Comparing Fig. 13 to the corresponding figure where an adiabatic assumption is used, the peak temperature in the case of no heat loss is higher. The peak current density in the case of no heat loss is lower but only slightly ($\sim$5 mA/cm^2). The overall current density distribution is slightly flatter in the heat loss case as the peak PEN temperature has moved toward the center of the cell. The PEN temperature distribution shows a steep drop at the fuel inlet and air inlet (fuel exit). At the fuel inlet the result is a large thermal gradient of 124 K/cm, which is larger than the gradient seen at the fuel exit. This is due to the additional cooling there resulting from the heat loss. Despite this steep drop, the total cross cell temperature difference remains close to that of the corresponding no heat loss case. However, this steep temperature drop may still introduce large thermal stresses that are of concern.

Similar trends are exhibited as the heat lost temperature is decreased further to 850 K. That is, the PEN temperature gradient at the fuel inlet increases to 157 K/cm, the peak cell temperature drops to 1158 K, and the location of the peak cell temperature moves further toward the center of the cell.

Dynamic Simulation Results. Previous sections of this paper have focused upon the steady-state model performance and sensitivity analyses. Importantly, the current model solves dynamic equations enabling spatially resolved dynamic SOFC simulation, which is essential to control systems development. To demonstrate dynamic simulation capabilities, the model was subjected to a 45% power increase while maintaining constant fuel and air utilization. The fuel and air inlet temperatures were held constant at
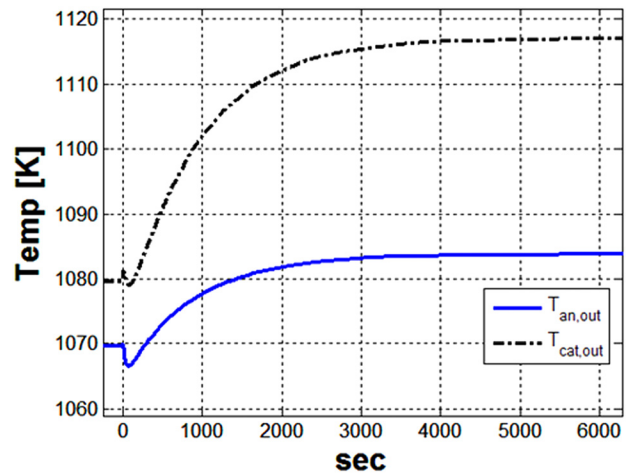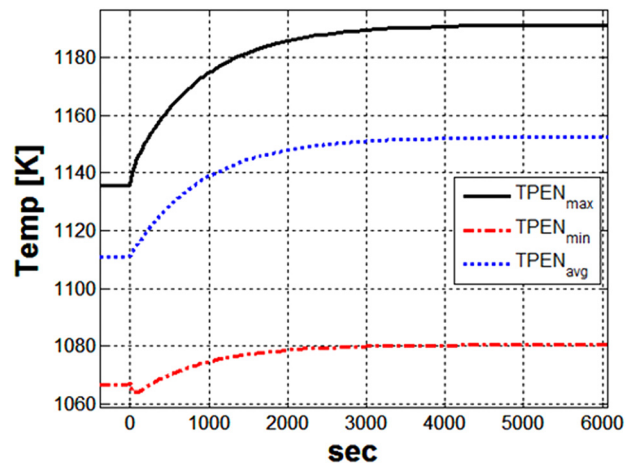
973 K during this power transient. This 45% power increase perturbation was accomplished by ramping power demand from the cell over a 2 s time interval. The fuel composition consisted of methane and steam with a steam to carbon ratio of 3. Figure 14 shows the power demand increase perturbation considered and the responses of the current density and voltage.

The thermal response of the fuel cell to the power transient is illustrated in Figs. 15 and 16. Both figures show that it takes around 3000 s for the fuel cell temperatures to reach 98% of their final steady state values. The cathode gas exit temperature actually experiences a slight ($\sim$2–3 K) temperature increase during the 2 s ramp up in power. This is a result of decreased residence times of the gases within the cathode compartment due to the increase in cathode air flow rate. The cathode exit temperature then begins to decrease for a short period ($\sim$70 s) as the PEN temperature near the fuel inlet begins to decrease as a result of the increased fuel flow and the resulting increased endothermic reformation reactions. The anode exit temperature in this timeframe also experiences a decrease after the power transient because of the decreased PEN temperatures near the cathode inlet and increased endothermic steam reforming reactions (near the fuel inlet). Figure 16 shows that the minimum PEN temperature near the fuel inlet drops temporarily during the initial transient response. This is followed by an overall rise in PEN temperatures due to increased heating of the cell assembly by higher power density operation.
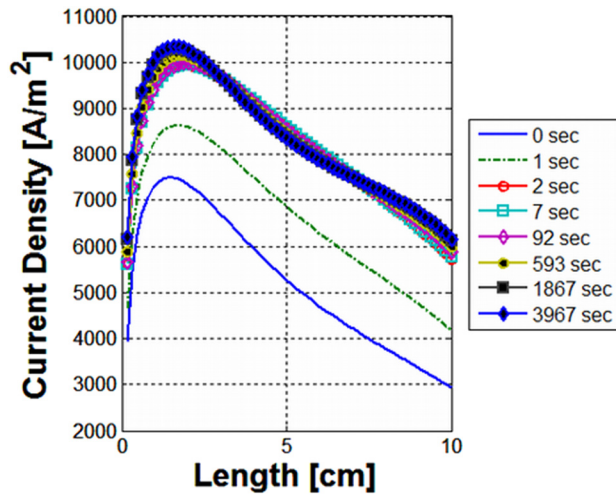
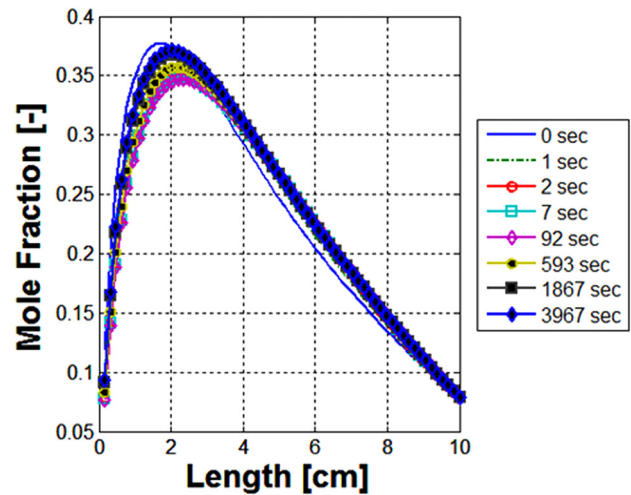Fig. 17 Response of current density distribution to the 45% power increase

Fig. 19 Response of hydrogen concentration distribution to the 45% power increase
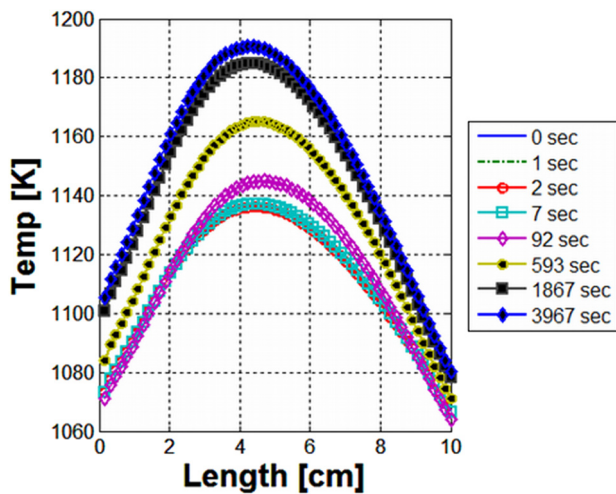

Fig. 18 Response of PEN temperature distribution to the 45% power increase for 4000 s after the dynamic
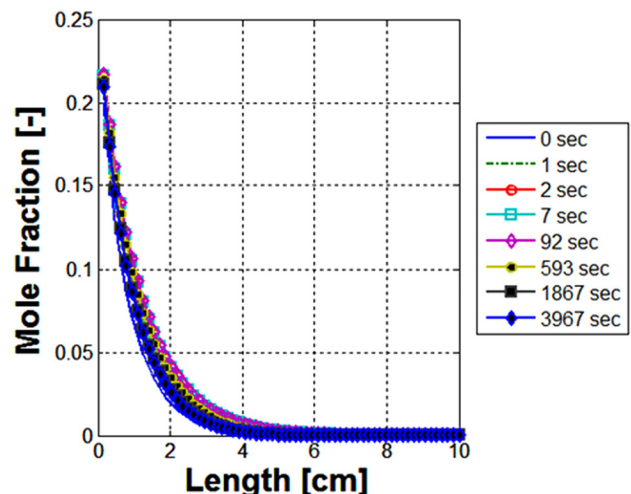

Fig. 20 Response of methane concentration distribution to the 45% power increase

The current density distribution during the transient is shown in Fig. 17. The current density distribution changes quickly as is expected from electrochemical and cell flow residence time scales. The peak in the current density distribution moves to a different axial position 7 s after the transient began. The peak then moves in the direction of air flow (toward 0 cm) as the cell temperatures increase such that the peak is very near the peak location before the transient. The movement of this peak is a result of the PEN temperature and hydrogen concentration distributions. From Figs. 18 and 19, it can be seen that the peak in PEN temperature and hydrogen concentration distributions move in the same fashion, i.e., first toward the anode exit (10 cm) and then back toward the anode inlet (0 cm) such that the peaks nearly line up with their location prior to the transient. At 7 s after the transient, the concavity of the current density distribution at an axial position of 6 cm also changes slightly during the transient from an upward to a downward concavity. The change in the concavity is also a result of the changes in the PEN temperature and hydrogen concentration distributions.

The response of the methane concentration distribution to the power transient is shown in Fig. 20. The methane concentration initially increases as a result of the increased fuel flow to maintain constant fuel utilization. After several hundred seconds, the methane concentration begins to move back toward its initial concen-

tration profile before the transient because of the rising PEN temperatures near the cell edges which leads to increased steam reforming reaction rates, commensurate with the increased fuel flow and power demand. Note that the time scale associated with the methane concentration distribution is on the order of several hundred seconds because it results from the coupled dynamics of chemical and electrochemical reactions, heat transfer and overall thermal response of the cell to the power demand increase perturbation.

Summary and Conclusions

A quasi-2-dimensional dynamic model has been developed to study on-anode reforming of methane in a planar SOFC. Continued improvements in the performance of SOFCs will have an effect on the temperature gradients within the SOFC PEN. Current results show that when the performance of the cell was improved, the resulting PEN temperature differential (ΔT_{PEN}) was increased by about 30 K for all of the fuel compositions considered. The sensitivity analyses presented herein suggest that cell temperature differentials will become even larger as manufacturers make the cells larger. Current results suggest that it may be possible to mitigate PEN temperature gradients by implementing effective controls and safeguards, but also by designing the stack with specific

features that can reduce ΔT_{PEN}. This could involve effective combinations of rib width, interconnect thickness, and interconnect material properties. Sensitivity of ΔT_{PEN} to heat losses to the environment shows that it is important to resolve cell edge heat loss effects. The spatially resolved dynamic simulation capability of the model was demonstrated for a 45% power increase perturbation while maintaining constant air and fuel utilizations. The simplified geometric resolution and dynamic capabilities of this model allow its use in system models used for controls development.

Acknowledgment

Nomenclature

A = surface area: m^2
C = specific heat: kJ/(kg $\cdot$ K)
D_c = characteristic diameter: m
E_0 = ideal voltage: V
E_q = activation energy: kJ/kmol
$\dot{E}$ = energy rate: kW
F = Faraday's constant: 96,485 kC/kmol
Δg = change in Gibbs free energy of reaction: kJ/kmol
$\dot{H}$ = enthalpy rate: kW
H = convection coefficient: kW/(m^2 $\cdot$ K) or Specific enthalpy: kJ/kmol
i = electrical current: kA
i_0 = exchange current density: kA/m^2
i_L = limiting current density: kA/m^2
j = current density: kA/ m^2
L = length: m
K = thermal conductivity: kW/(m $\cdot$ K)
k_0 = pre-exponential constant: kmol/(m^2-s-bar)
K_{eq} = equilibrium constant
M = molar mass: kg/kmol
N = mole number: kmol
$\dot{N}$ = molar flow rate: kmol/s
Nu = Nusselt number
N = electron coefficient ratio
P = pressure: kPa, bars
Q = reaction quotient
$\dot{Q}$ = heat transfer rate: kW
R = reaction rate: kmol/s or resistance: Ω
R_u = universal gas constant: 8.314 kJ/(kg-K)
T = temperature: K
ΔT = change in temperature: K
T = time: s
U = internal energy: kJ
U = specific internal energy: kJ/kg
V = voltage: V or volume: m^3
$\dot{W}_{elec}$ = electrical power: kW
X = species mole fraction
E = efficiency
H = polarization: V
P = density: kg/m^3
N = stochiometric coefficient

Acronyms

LHV = lower heating value
SC = steam-to-carbon
PEN = positive electrode-electrolyte-negative electrode
SOFC = solid oxide fuel cell
HP = high performance
LP = low performance

References

[1] Vora, S. D., 2010, "Office of Fossil Energy Fuel Cell Program—Solid State Energy Conversion Alliance (SECA) Clean Economic Energy for a Carbon Challenged World," Proceedings of the 11th Annual SECA Workshop, July 27–29, Pittsburgh, PA.
[2] Sangtongkitcharoen, W., Assabumrungrat, S., Pavarajarn, V., Laosiripojana, N., and Praserthdam, P., 2005, "Comparison of Carbon Formation Boundary in Different Modes of Solid Oxide Fuel Cells Fueled by Methane," J. Power Sources, 142, pp. 75–80.
[3] Laosiripojana, N., and Assabumrungrat, S., 2007, "Catalytic Steam Reforming of Methane, Methanol, and Ethanol Over Ni/YSZ: The Possible Use of These Fuels in Internal Reforming SOFC," J. Power Sources, 163, pp. 943–951.
[4] Ferguson, J. R., Fiard, J. M., and Herbin, R., 1996, "Three-Dimensional Numerical Simulation for Various Geometries of Solid Oxide Fuel Cells," J. Power Sources, 58(2), pp. 109–122.
[5] Mueller, F., Brouwer, J., Jabbari, F., and Samuelsen, S., 2006, "Dynamic Simulation of an Integrated Solid Oxide Fuel Cell System Including Current-Based Fuel Flow Control," J. Fuel Cell Sci. Technol., 3, pp. 144–154.
[6] Daun, K. J., Beale, S. B., Liu, F., and Smallwood, G. J., 2006, "Radiation Heat Transfer in Planar SOFC Electrolytes," J. Power Sources, 157(1), pp. 302–310.
[7] Tanaka, T., Inui, Y., Urata, A., and Kanno, T., 2007, "Three Dimensional Analysis of Planar Solid Oxide Fuel Cell Stack Considering Radiation," Energy Convers. Manage., 48(5), pp. 1491–1498.
[8] Achenbach, E., 1994, "Three-Dimensional and Time-Dependent Simulation of a Planar Solid Oxide Fuel Cell Stack," J. Power Sources, 49(1), pp. 333–348.
[9] Kim, J. W., Virkar, A. V., Fung, K. Z., Mehta, K., and Singhal, S. C., 1999, "Polarization Effects in Intermediate Anode Supported Solid Oxide Fuel Cells," J. Electrochem. Soc., 146(1), pp. 69–78.
[10] Xu, J., and Froment, G., 1989, "Methane Steam Reforming, Methanation, and Water Gas Shift: I. Intrinsic Kinetics," AIChE J., 35, pp. 88–96.
[11] Aguiar, P., Adjiman, C. S., and Brandon, N. P., 2004, "Anode-Supported Intermediate Temperature Direct Internal Reforming Solid Oxide Fuel Cell. I: Model-Based Steady-State Performance," J. Power Sources, 138, pp. 120–136.
[12] Achenbach, E., and Riensche E., 1994, "Methane/Steam Reforming Kinetics for Solid Oxide Fuel Cells," J. Power Sources, 52, pp. 283–288.
[13] Ahmed, K., and Foger, K., 2000, "Kinetics of Internal Steam Reforming of Methane on Ni/YSZ-Based Anodes for Solid Oxide Fuel Cells," Catal. Today, 63(2-4), pp. 479–487.
[14] Iora, P., Aguiar, P. Adjiman, C. S., and Brandon, N. P., 2005, "Comparison of Two IT DIR-SOFC Models: Impact of Variable Thermodynamic, Physical, and Flow Properties. Steady-State and Dynamic Analysis," Chem. Eng. Sci., 60(11), pp. 2963–2975.
[15] Incropera, F., and DeWitt, D., 2002, Fundamentals of Heat and Mass Transfer, 5th ed., John Wiley & Sons, Inc., Hoboken, NJ.
[16] Ghezel-Ayagh, H., 2008, "Solid Oxide Fuel Cell Program at FCE, Inc.," Proceedings of the 9th Annual SECA Workshop, August 5–7, Pittsburgh, PA.
[17] Leone, P., Santarelli, M., Asinari, P., Cali, M., and Borchiellini, R., 2008, "Experimental Investigations of the Microscopic Features and Polarization Limiting Factors of Planar SOFCs With LSM and LSCF Cathodes," J. Power Sources, 177(1), pp. 111–122.
[18] Laurencin, J., Lefebvre-Joud, F., and Delette, G., 2008, "Impact of Cell Design and Operating Conditions on the Performances of SOFC Fuelled With Methane," J. Power Sources, 177(2), pp. 355–368.